

Sensitivity and Variability Redux in Hot-Jupiter Flow Simulations

J. Y-K. Cho,^{1,2*} I. Polichtchouk,^{1,3} H. Th. Thrastarson,⁴

¹ School of Physics and Astronomy, Queen Mary University of London, London E1 4NS, UK

² Institute for Theory and Computation, Harvard University, Cambridge, MA 02138, USA

³ Department of Meteorology, University of Reading, Reading RG6 6BB, UK

⁴ Jet Propulsion Laboratory, California Institute of Technology, Pasadena, CA 91109, USA

Accepted yyyy mmm dd. Received yyyy mmm dd; in original form yyyy mmm dd

ABSTRACT

We revisit the issue of sensitivity to initial flow and intrinsic variability in hot-Jupiter atmospheric flow simulations, originally investigated by Cho et al. (2008) and Thrastarson & Cho (2010). The flow in the lower region (~ 1 to 20 MPa) ‘dragged’ to immobility and uniform temperature on a very short timescale, as in Liu & Showman (2013), leads to effectively a complete cessation of variability as well as sensitivity in three-dimensional (3D) simulations with traditional primitive equations. Such momentum (Rayleigh) and thermal (Newtonian) drags are, however, ad hoc for 3D giant planet simulations. For 3D hot-Jupiter simulations, which typically already employ strong Newtonian drag in the upper region, sensitivity is not quenched if only the Newtonian drag is applied in the lower region, without the strong Rayleigh drag: in general, both sensitivity and variability persist if the two drags are not applied concurrently in the lower region. However, even when the drags are applied concurrently, vertically-propagating planetary waves give rise to significant variability in the ~ 0.05 to 0.5 MPa region, if the vertical resolution of the lower region is increased (e.g. here with 1000 layers for the entire domain). New observations on the effects of the physical setup and model convergence in ‘deep’ atmosphere simulations are also presented.

Key words: hydrodynamics – turbulence – methods: numerical – planets: atmospheres.

1 PROLEGOMENON

Many studies have explored the effects of initial condition and resolution or dissipation in hot-Jupiter atmospheric flow simulations (e.g. Cho et al. 2008; Thrastarson & Cho 2010; Heng, Menou & Phillipps 2011; Thrastarson & Cho 2011; Polichtchouk & Cho 2012; Bending, Lewis & Kolb 2012; Liu & Showman 2013; Polichtchouk et al. 2014). Thrastarson & Cho (2010) [hereafter TC], in particular, have emphasised the nonlinear effect of initial jet configuration on the subsequent evolution, calling attention to it as a source of uncertainty for *quantitative* predictions. ‘Quantitative’ here means such things as the precise location of hot regions and the three-dimensional (3D) shape and magnitude of vortices and jets, which affect the *directly-coupled* temperature distribution as well as the wave momentum and energy depositions. Similar emphasis has also been made by Cho et al. (2008) in the two-dimensional (2D) context with initial turbulent eddies, in which strength of the eddies affected the final mean flow configuration. In this paper we revisit the effects with the commonly-used traditional (i.e. hydrostatic) primitive equations with extended, ‘deep’ vertical domain.¹

* On leave from QMUL; Email: J.Cho@qmul.ac.uk

¹ The discussion here, however, is also germane to understanding results from simulations with the compressible, non-hydrostatic, 3D Navier–Stokes equations (e.g. Dobbs-Dixon & Lin 2008; Mayne et al. 2014).

Recently, Liu & Showman (2013) [hereafter LS] have performed a set of 3D traditional primitive equations simulations with specified thermal (Newtonian) and momentum (Rayleigh) drags and assert that TC observe sensitivity because they fail to meet a presumptive setup criteria for ‘real’ hot-Jupiters (LS, p. 48).² In their work, LS also advocate the use of a strong Rayleigh drag in a fiducial region (denoted as \mathcal{D} in this paper) at the bottom of the modelled atmosphere. Here by ‘strong’ we mean a specified Newtonian or Rayleigh drag with a timescale of few (or less) planetary rotations; and, \mathcal{D} is defined as the pressure range, $p = [1, 20]$ MPa³, where both drags are ‘turned on’ in LS. In this paper, we clarify the situation: the insensitivity occurs in LS because the combined, strong Newtonian and Rayleigh drags suppress effectively *all* dynamics, everywhere in the domain, except for laminar high-speed jets. Quantitative features of the flow, as defined above, are sensitive to initial conditions when the strong drags are not applied.

² LS also emphasise that the equilibrium temperature and relaxation time profiles in TC are constant. However, as stated in TC and explicitly shown in Polichtchouk et al. (2014), the sensitivity and variability persist under vertically-varying equilibrium temperature distribution and relaxation-timescale that match closely with those used in LS, *over the domains considered in TC and Polichtchouk et al. (2014)*.

³ 1 MPa = 10 bars

Rayleigh drag, which is often used to crudely represent a physical boundary layer in 3D simulations of large-scale flows (e.g. Held & Suarez 1994), is implausible for the \mathcal{D} region of a giant planet without a ‘solid’ surface or with one located deep in its interior – particularly if the drag is a strong one.⁴ The use of such a drag in \mathcal{D} is notable given that past hot-Jupiter studies without the drag have already reported a lack of sensitivity and variability (e.g. Showman et al. 2009; Cooper & Showman 2005): hence, it is not required per se to demonstrate insensitivity. Nonetheless, to elucidate the effects of the new setup with strong drags, we set up here simulations as in LS and cross-check the results with several different codes. In doing so, we explicitly demonstrate that the sensitivity is quenched only under the application of an unphysical, strong Rayleigh drag and that such a drag is not necessary for attaining equilibration if a strong Newtonian drag is already applied.⁵ In any case, ‘equilibration’ reached – with or without the drag – is best regarded as heuristic and should not be taken too literally in the present setup because unphysical supersonic flow results from it. Even with both drags applied, variability and weak sensitivity persist if vertical resolution of the \mathcal{D} region is increased in the simulations.

2 SETUP

TC and LS solve the traditional primitive equations (e.g. Holton 2004) with the same, or effectively the same, boundary conditions (zero ‘vertical velocity’ – i.e. ‘free slip’ – at the top and bottom of the domain).⁶ However, the basic numerical algorithm, treatment of explicit viscosity and vertical coordinate are all very different: in TC pseudospectral and superviscosity with CAM (Collins et al. 2004) in η -coordinate and in LS finite-volume and moderate-order Shapiro filter with MITgcm (Adcroft et al. 2012) in p -coordinate, with the vertical layers equally spaced in $\log(p)$. In this study, we solve the same equations with the free-slip boundary conditions; but, unlike in TC and LS, we employ *both* the pseudospectral and finite-volume models. While the latter is the same model, grid configuration (cubed-sphere) and vertical coordinate used in LS, the former is different than the model used in TC: the BOB model (Scott et al. 2004) in p -coordinates, with vertical layers equally spaced in $\log(p)$ and p , is used here. BOB is purposely chosen to provide an independent check of TC’s results, as well as those of LS. Note that, in general, models employing the pseudospectral algorithm converge much faster with resolution than models using finite-volume algorithms (see e.g. Polichtchouk et al. 2014, as well as the discussion below).

In all three studies (TC, LS and the present one), planetary parameter values characteristic of the hot-Jupiter HD209458b are used (see TC for the values). In this paper, all times and lengths are

⁴ Recently, Schneider & Liu (2009) have put forth a weak Rayleigh drag representation of ‘magnetohydrodynamics-induced drag’ effect, but the representation is at present not widely accepted.

⁵ The latter point was not made explicit in TC and some confusion appears to exist concerning ‘equilibration’ under strong, planetary-scale Newtonian drag – perhaps unduly influenced by barotropic non-divergent (i.e. incompressible 2D) turbulence formalism, which does not involve the thermodynamic fields.

⁶ MITgcm has an option to allow the bottom pressure surface to be free (i.e. nonzero vertical velocity). The state of this option is not specified in LS; but, the results are not noticeably affected by the option for the setup as in LS. However, in general, energy is added and stability is affected with the option on. The option is off in all the simulations discussed in this paper.

scaled by the planetary rotation period ($\tau = 3.024 \times 10^5$ s) and radius ($\mathcal{L} = 10^8$ m), respectively – unless units are explicitly given. Hence, $t = 1$ corresponds to 1 HD209458b day. Also in all three studies, the thermal forcing is crudely represented by a relaxation (drag) to a specified ‘equilibrium’ temperature distribution $T_e(\lambda, \phi, p)$ with a drag-time profile $\tau_N(p)$; here λ is longitude and ϕ is latitude.

Note that T_e and τ_N are not same in TC and LS, as stressed by LS. But, they are not very different: the difference is no more than few percent over the model domain in some of the simulations reported in TC and all of the forced simulations in Polichtchouk et al. (2014), which uses one of the vertically-varying profiles from the TC study. In the present study, the profile $T_e(p)|_{\lambda, \phi}$ is also not precisely (but essentially) same as that in LS: the profile in LS is represented as continuous, piece-wise linear functions in three distinct p regions, as τ_N is in LS.⁷ Also, our τ_N in \mathcal{D} is 10^6 s ($= 3.3$ scaled), rather than 10^7 s, independent of p . The smaller value is as in Fig. 6 of LS, and in simulations presented in most of their discussion. However, with both drags applied in \mathcal{D} , insensitivity to initial flow does not depend on whether the p -independent τ_N in \mathcal{D} is 10^6 s or 10^7 s. In fact, as demonstrated below, none of the above differences in the physical setup are pertinent to the question of sensitivity: only the Rayleigh drag, as employed in LS, is pertinent.

The crucial Rayleigh drag is characterised by the drag-time profile $\tau_R(p)$. Note that, in all the simulations discussed in this paper, the Rayleigh drag is applied only in the vertical region, $\log(p) = [5.0, 7.3] = [5.0, 6.0] \cup \mathcal{D}$, with $\tau_R(p)$ decreasing exponentially with $\log(p)$ – i.e. linearly with p . The specification is as in LS. When the drag is not applied in \mathcal{D} , it is not applied anywhere in the domain. The strength of the p -dependent τ_R is characterised by $\min\{\tau_R(p \in \mathcal{D})\} = \tau_R(20 \text{ MPa})$, and denoted τ_{R20} here.

3 RESULTS

Fig. 1 summarises one of the basic results of this paper: without the ad hoc strong drags applied in \mathcal{D} , sensitivity to initial flow is robust. The figure shows time-averaged, zonal-mean zonal velocity $\bar{u}^*(\phi, p)$ from four pairs of simulations with identical setup – except for the direction of the initial, barotropic zonal jet (see TC for details of the jet profiles) and the presence or absence of both Newtonian and Rayleigh drags in \mathcal{D} . In Fig. 1a and 1b, τ_N and τ_R are as in the simulations of LS that apply both drags. In Fig. 1c and 1d, τ_N is as in LS outside \mathcal{D} , but with $\tau_N, \tau_{R20} \rightarrow \infty$ inside \mathcal{D} (i.e. the Newtonian drag is not applied in \mathcal{D} and the Rayleigh drag is not applied anywhere in the domain). Simulations in Fig. 1a and 1c are performed with BOB (T85L40 resolution; timestep size, $\Delta t = 2 \times 10^{-4}$; and, 8th-order hyperviscosity coefficient, $\nu_8 = 1.5 \times 10^{-13}$), and simulations in Fig. 1b and 1d are performed with MITgcm using the energy-conserving vorticity advection scheme (C64L40 resolution; $\Delta t = 10^{-4}$; Shapiro filter order, $n = 4$; and, filter strength ratio, $\Delta t / \tau_{shap} = 0.25$, where τ_{shap} is the Shapiro filter coefficient).⁸ Here ‘T85L40’ denotes 40 vertical layers with 85 total and 85 sectoral spherical harmonic modes in the Legendre expansion per layer, and ‘C64L40’ denotes 40 vertical layers with $6 \times 64 \times 64$ grid points per layer (see Polichtchouk et al. 2014, for details of the models).

Several features are readily apparent in Fig. 1. First, the East

⁷ N.B. τ_N here is ‘ τ_{rad} ’ in LS.

⁸ Note that MITgcm can be sensitive to the numerical parameter values, as we discuss later; hence, simulations that match most closely with the BOB simulations are presented.

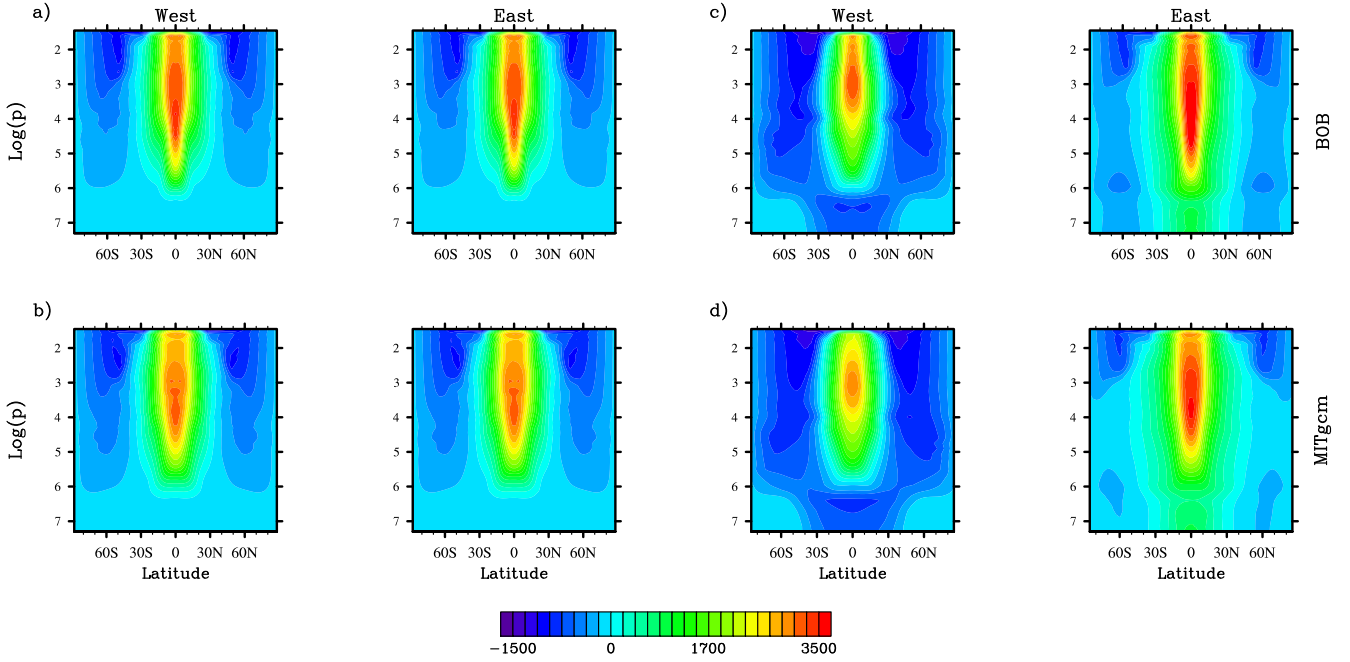


Figure 1. Time-averaged (over $t = [250, 300]$), zonal-mean zonal velocity $\bar{u}^*(\phi, p)$, where ϕ is latitude and p is pressure, from simulations initialised with $\pm 1000 \text{ m s}^{-1}$ (East/West) equatorial jet. Simulations in a) and c) are performed with BOB and in b) and d) are performed with MITgcm in cubed-sphere grid. All simulations are performed with vertical layers equally-spaced in $\log(p [\text{Pa}])$. In a) and b), $\tau_N = 3.3$ independent of $\log(p)$ and τ_R in \mathcal{D} decreases exponentially with $\log(p)$ for $p > 0.1 \text{ MPa}$ with $\tau_{R20} = 3.3$. In c) and d), both $\tau_N, \tau_R \rightarrow \infty$ in \mathcal{D} (i.e. no drags in \mathcal{D}); hence, $\tau_{R20} \rightarrow \infty$. When both drags are applied, \bar{u}^* is essentially same, irrespective of the initial jet direction [a) and b)]; when both drags are not applied, \bar{u}^* is strongly dependent on the jet direction [c) and d)].

and West BOB simulations in Fig. 1a show no practical difference between them, in agreement with LS using the MITgcm. Second, not only do the East and West MITgcm simulations in Fig. 1b also show no practical difference between them, they match very well with the corresponding BOB simulations in Fig. 1a. The match is not exact, however, and we shall return to this point shortly. For now the salient point we wish to make is that the MITgcm results here are nearly identical to those presented in LS⁹: hence, there is no issue with the aforementioned minor difference in T_e or with the numerical parameter values chosen for the MITgcm simulations in this study. Third, as seen in Fig. 1c and 1d, when the strong drags are not imposed in \mathcal{D} , the \bar{u}^* distributions in the East and West simulations are clearly distinct – even when the data is heavily averaged, as in the figures. Grossly speaking, there are three jets in both, East and West simulations, but the width, strength and vertical structure of the jets are all noticeably different. Observe as well that the East and West simulations in Fig. 1c (and Fig. 1d) separately do not match the corresponding East and West simulations in Fig. 1a (and Fig. 1b) – particularly below $\log(p) \approx 3$ and away from the equatorial region. According to the figure, there are at least three plausible states, depending on the setup and initial condition.

The first two features above confirm simultaneously the BOB simulations in this study and the MITgcm simulations in LS. The very good agreement between the two models (cf. Fig. 1a and 1b) is significant, as this is the first time extrasolar planet atmospheric flow simulations from two different numerical models are shown explicitly to produce nearly *quantitatively* same results over the en-

tire domain – results which are numerically converged over a good range of parameter values. In general, significant variations in the simulation results are observed across different models, as well as within a single model (see e.g. Polichtchouk et al. 2014; Thrastarsson & Cho 2011, and the discussion below). It is imperative to understand, however, that the good agreement here is due to the highly constraining setup. Nevertheless, as already pointed out, the agreement is still not exact: the equatorial jets in Fig. 1a are faster and sharper than those in Fig. 1b, especially outside $\log(p) \approx [3.3, 4.3]$. LS report that in some cases modest variability is exhibited but sensitivity is not exhibited, after the simulation reaches the statistically steady state. We have found that this is the case with the setup as in Fig. 1a and 1b.

The third feature confirms the behaviour reported in TC: the flow is sensitive to the initial state. In particular, it demonstrates explicitly that the sensitivity observed in TC does not depend on whether the day-night thermal gradient extends all the way down, or only part way down, to the bottom of the domain. LS speculate that the sensitivity in TC may be caused by a global-scale baroclinic instability induced by the gradient present at the bottom of the domain. However, TC have reported sensitivity in a variety of setup, including one with reduced equilibrium temperature gradient at the bottom. Moreover, Polichtchouk & Cho (2012) have explicitly shown that, if a flow is baroclinically unstable, the instability is not thwarted by adding inactive layers (or drags) *below* the unstable region. Hence, the placement of the bottom boundary is not the crucial factor for sensitivity in these studies. However, such factors (including numerous other physical and numerical ones) can in fact affect instabilities or wave dynamics that naturally arise in the course of the flow evolution, steering it to different regions of

⁹ cf. with Fig. 8 in LS, modulo plot aspect ratio and minor differences in the color range and palette

the configuration (solution) space – and, this is so even if simulations begin with identical initial conditions (e.g. Polichtchouk & Cho 2012; Thrastarson & Cho 2011). The point here is that the state illustrated in Fig. 1a (and 1b) is an extraordinary one.

Interestingly, behaviour similar to that in Fig. 1c and 1d can also be seen in the correspondingly-similar simulations of LS (see Fig. 15 therein, bottom row¹⁰). But, LS interpret the behaviour as ‘artificial’ because the total angular momentum does not converge to the same value. We note here that there is no a priori reason why this measure needs to be the same among *different* model instantiations with different initialisation and balance.¹¹; in addition, even if the measure is same, the spatial distribution of the flow (and thus temperature) need not be same.¹² Indeed, this had been precisely TC’s point and that of Cho et al. (2008), as well as the present paper: the (unknown) magnitude and distribution of angular momentum and eddy kinetic energy in the actual atmosphere – needed for model initialisation – lead to divergent model evolutions, preventing any kind of precise quantitative predictions at present.

At this point, we briefly discuss an important numerical issue: we have found that MITgcm simulations suffer significant runaway angular momentum and acute sensitivity to numerical parameters, when both drags are not employed (Fig. 1d). An extensive study of angular momentum conservation in several numerical models has been performed and is described elsewhere (Polichtchouk & Cho, in prep.). The basic issue is illustrated in Fig. 2, in which time series of mass-weighted, global-average, axial angular momentum M for simulations with Eastward-jet and Westward-jet initialisations at different resolutions are presented¹³; each series is normalised by its initial value, $4.34 \times 10^{34} \text{ kg m}^2 \text{ s}^{-1}$ for the East simulations and $2.76 \times 10^{34} \text{ kg m}^2 \text{ s}^{-1}$ for the West simulations. Fig. 2a shows the runaway and sensitivity (with resolution) in MITgcm simulations. The runaway and sensitivity reduce at high resolution (e.g. at C64), but do not vanish. In contrast, runaway and sensitivity are not observed in BOB simulations, as seen in Fig. 2b. The runaway is detectable in Fig. 1: notice the small north–south hemispherical symmetry breaking in Fig. 1d, but not in Fig. 1c. Since external symmetry breaking has not been introduced in these simulations, the asymmetry is a manifestation of the runaway – i.e. a numerical error. Hence, total angular momentum is not a useful measure for MITgcm in this case; and, BOB and CAM results (which are in good agreement with each other) cannot be robustly reproduced or tested with MITgcm when strong drags are not applied in \mathcal{D} .

Given the zonal and temporal averaging in Fig. 1, it may be difficult to fully appreciate just how different the fields can be in simulations initialised with different jets when the strong drags are not applied in \mathcal{D} . Unaveraged fields contain more information and are more useful for comparing with observations. Fig. 3 shows the instantaneous flow and temperature fields from the East and West simulations of Fig. 1c at the levels, $\log(p) = \{2.0, 4.0, 5.6, 7.0\}$, at

¹⁰ Note, the Newtonian drag is employed in \mathcal{D} here, unlike in Fig. 1c and 1d; but, the inclusion of the Newtonian drag is not pertinent to the present discussion, as shown below.

¹¹ Here ‘balance’ refers to the degree of vortical mode dominance (over gravity wave mode) of the flow field (e.g. Ford, McIntyre & Norton 2000).

¹² See Polichtchouk et al. (2014); this can also be inferred from the East and West pairs of simulations in Fig. 2b, presented below, in which the flow and temperature fields are markedly different despite starting with (and maintaining) same values of global angular momentum.

¹³ $M = (R_p/g) \int_{\mathfrak{V}} (\Omega R_p \cos \phi + u) \cos \phi dV$, where Ω is the rotation rate of the planet, R_p is the radius of the planet, g is the gravity, u is the zonal velocity, dV is the volume element and \mathfrak{V} is the global domain.

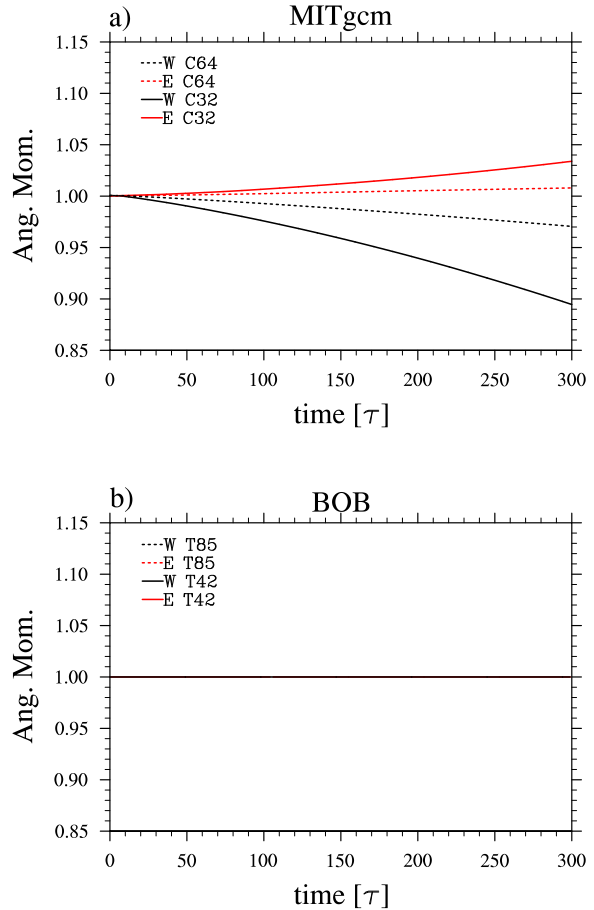


Figure 2. Mass-weighted, global-average, axial angular momentum [$\text{kg m}^2 \text{ s}^{-1}$] time series for simulations with East(E)/West(W) initialisations at different resolutions. Each series is normalised to its initial value: $4.34 \times 10^{34} \text{ kg m}^2 \text{ s}^{-1}$ (E) and $2.76 \times 10^{34} \text{ kg m}^2 \text{ s}^{-1}$ (W) simulations. The physical setup is as in Fig. 1d (MITgcm) and Fig. 1c (BOB). MITgcm exhibits monotonic runaway behaviour, which reduces with increased resolution. In contrast, the BOB model conserves angular momentum exactly, independent of the resolution.

$t = 300$. Both the flow and temperature distributions are markedly different in the two columns (East and West simulations), except near the top of the domain (cf. $\log(p) = 2$ frames). The behaviour near the top is expected, given the extremely strong Newtonian drag applied there ($\tau_N \approx 0.03$). But, even there significant differences are present in both fields, as will be shown more clearly below.

Significantly, there is much emphasis in the current literature on the temperature distribution at high altitude (e.g. $p = 30$ mbar $\Rightarrow \log(p) \approx 3.5$), where both the temperature and the flow are highly restrained by the very short τ_N (≈ 0.1). However, attention should also be given to the lower regions – for a more realistic, complete picture.¹⁴ First, note that such timescales are comparable to the Brunt–Väisälä period, the timescale of ‘deep’ internal gravity waves. The distortion or omission of various waves, including the gravity waves, is a source of significant inaccuracy in current atmospheric flow simulations: for example, wave interactions with the background flow (which modify the temperature distribution) are poorly captured – if at all (see e.g. Ford, McIntyre & Norton

¹⁴ This also applies to the mid- and high-latitude regions.

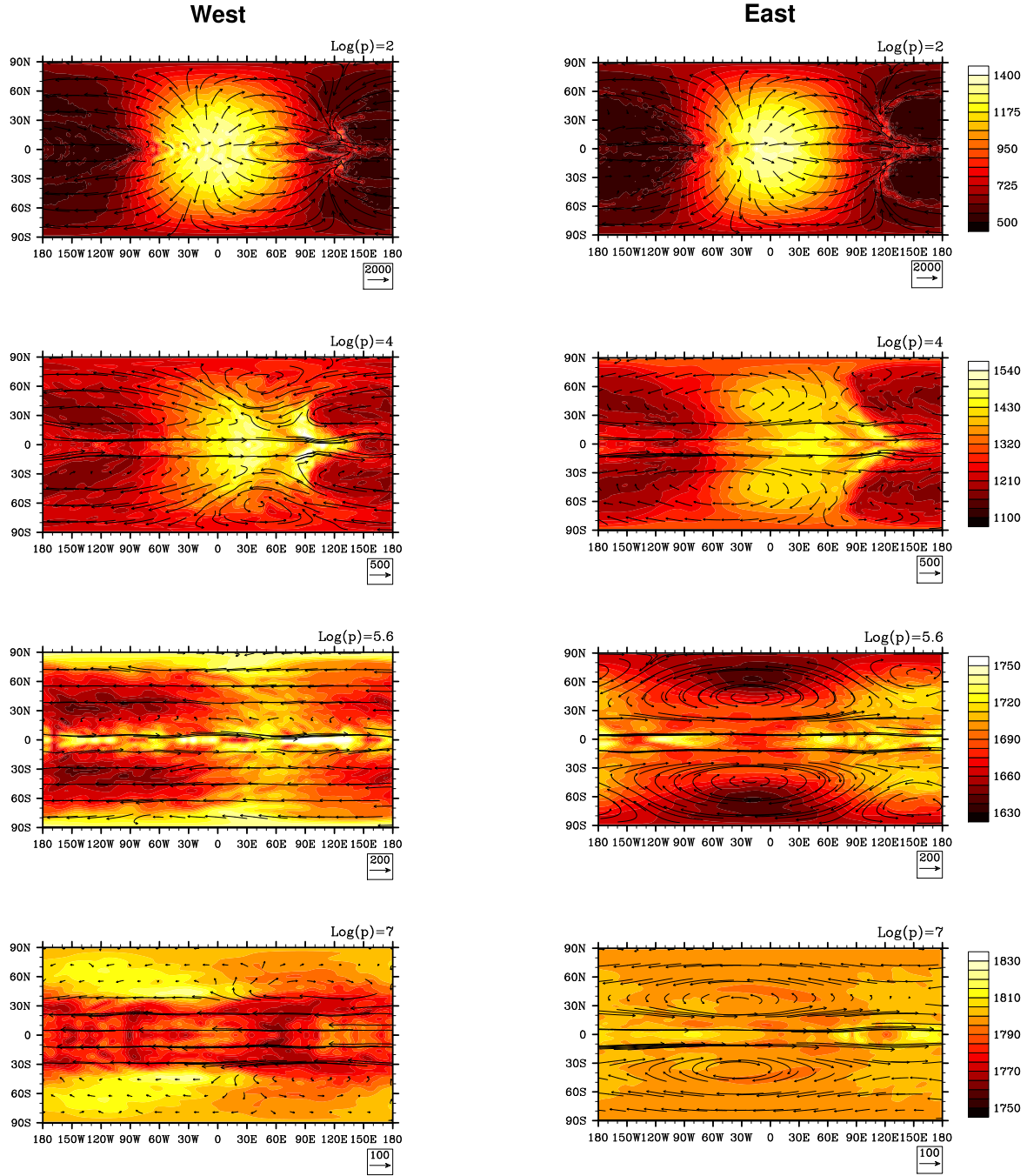


Figure 3. Instantaneous latitude–longitude maps of the flow \mathbf{v} (m s^{-1}) and temperature T (K) fields at four pressure levels, $\log(p) = \{2.0, 4.0, 5.6, 7.0\}$, at $t = 300$ in cylindrical-equidistant projection from the (West/East) simulations in Fig. 1c; $\mathbf{v} = (u, v)$, where u and v are the zonal and meridional velocities, respectively. The reference flow vectors are shown at the bottom right in each panel and temperature ranges for each row are shown at the right. In both West and East simulations, the flow and temperature distributions are complex with multiple, irregular hot/cold regions – often situated away from the equator and substellar/antistellar ($0^\circ/180^\circ$) longitude. The spatial distribution of the flow and temperature fields are significantly different, except near the top of the modelled domain (see Fig. 4). Symmetry has not been broken initially, unlike in most simulations in TC. The vertical temperature gradient fields in the two simulations are also different, and would lead to different emergent heat flux distributions.

2000; Cho et al. 2003; Watkins & Cho 2010, and also this study below). These interactions can be long-range and be effected by waves originally of small amplitude or scale. Second, infrared flux itself can originate from any of the levels modelled, consistent with the use of Newtonian relaxation approximation. The approximation is meant to represent crudely the effect of radiation emanating from

the atmospheric region where the approximation is being invoked (e.g. Salby 1996; Andrews et al. 1987; Cho et al. 2008). Given the above, matches with observations in current simulations may merely be fortuitous: a better understanding of both the physics and numerics is needed.

Note also that the fields in Fig. 3 are very similar to those in

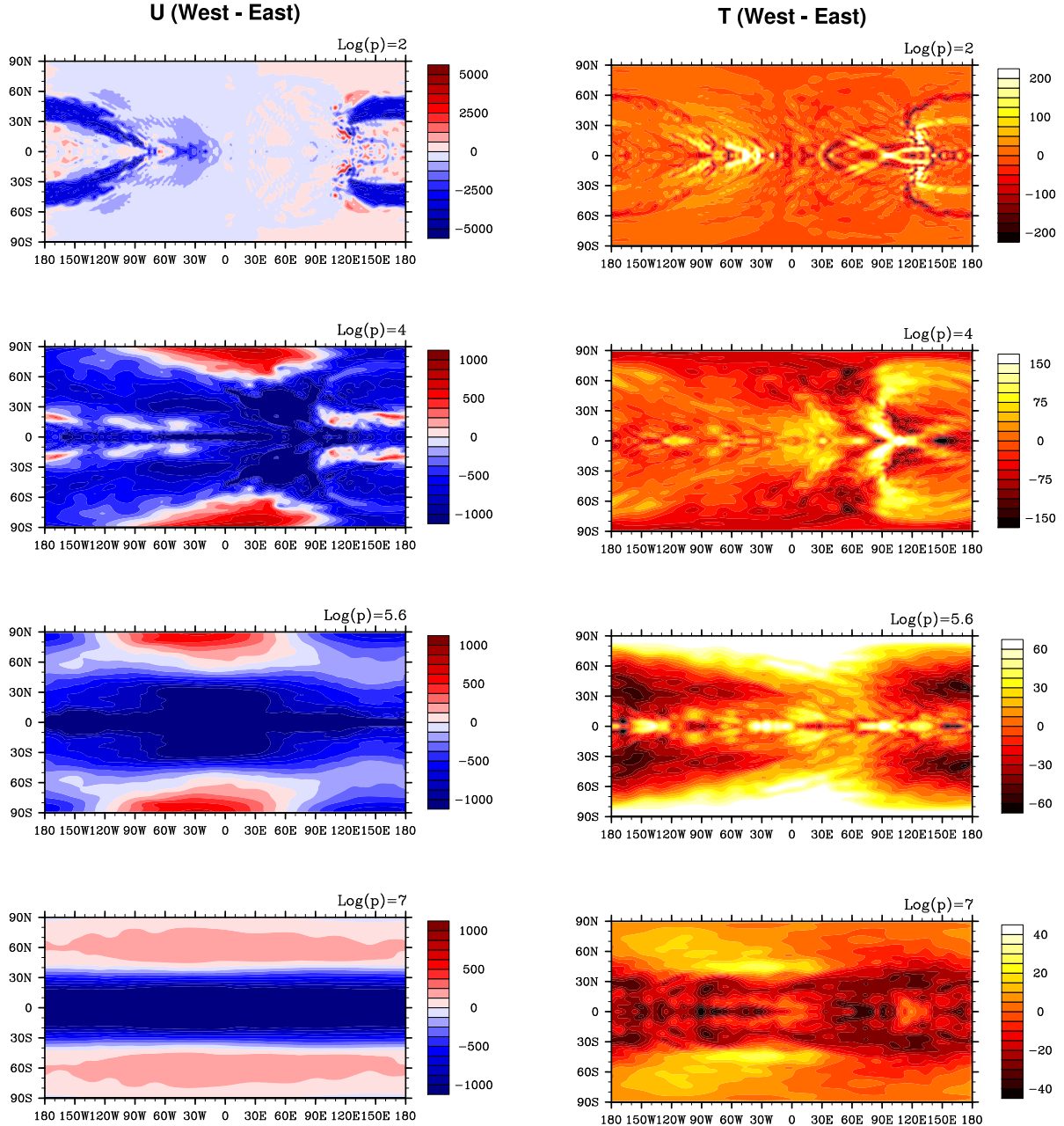


Figure 4. *West – East* difference maps of the zonal wind u (m s^{-1}) and temperature T (K) fields at the p -levels in Fig. 3. The wind differences are at the left column, and the temperature differences are at the right column. The plot ranges are shown at the right of each panel. Locally, the absolute flow and temperature differences can be large – as much as $\sim 4000 \text{ m s}^{-1}$ and $\sim 200 \text{ K}$ at $\log(p) = 2$, respectively.

TC, despite the bottom boundary being located at a much greater depth in the simulations of the figure. As in TC, the hottest and coldest regions are not simply connected (e.g. Munkres 2000) and often located away from the equator. This is in contrast to ‘maps’ constructed from observations which assume a latitudinal distribution monotonically decaying away from the equator. Moreover, the hottest (coldest) region can often be situated at the night (day) side, also in contrast to what has been reported in some observations and simulations (e.g. Knutson et al. 2007, LS, and references therein). In general, the locations of the temperature extremum regions vary in space and time, within a single simulation and across different simulations (e.g. Cho et al. 2003, 2008; Thrastarson & Cho 2010;

Polichtchouk et al. 2014), again depending on the initial flow and equilibrium temperature states specified.

For a clearer picture of the magnitude and spatial distribution of the *differences*, Fig. 4 presents point-wise subtractions of the West and East frames at the p -levels shown in Fig. 3. In Fig. 4, the left column shows the instantaneous zonal wind field difference, $u_w(\lambda, \phi) - u_E(\lambda, \phi)$, and the right column shows the instantaneous temperature field difference, $T_w(\lambda, \phi) - T_E(\lambda, \phi)$. Note the large, absolute maximum flow and temperature differences (more than $\sim 4000 \text{ m s}^{-1}$ and $\sim 200 \text{ K}$, respectively) locally at $\log(p) = 2$. At greater depths the u -differences are reduced, but are still quite large ($\sim 1000 \text{ m s}^{-1}$) and on global scales. The u -difference in

the left bottom panel reflects the opposite sign of the zonal jets in the \mathcal{D} region in the two simulations, particularly in the equatorial region (cf. East and West simulations in Fig. 1c, for example). The T -differences also generally decrease with depth. Notably, in the \mathcal{D} region, the temperature difference is a very small fraction of the ambient temperature ($\lesssim 4\%$) in both of the simulations, indicating that the Newtonian drag as specified in simulations of Fig. 1a and 1b is not really effective or needed. This is not surprising, given the large inertia of \mathcal{D} .

In their study, LS motivate the use of a strong Rayleigh drag in as an ‘accelerator’ to help reach the ‘equilibrium’ state more quickly. However, such a drag can steer the flow to artificial states and is in actuality unnecessary – particularly if temperature is used to characterise the equilibration, as in many climate studies (e.g. Brandefelt & Otto-Btiesner 2009), or if strong Newtonian drag is already applied in \mathcal{D} (which is also dubious, as noted above). Both can be clearly seen in Fig. 5, where time series normalised by the initial value from four long-duration simulations (roughly ‘permutations of $\{(\tau_{R20}, \tau_N)\}$ ’) are presented; all the simulations here employ strong Newtonian drag in the upper region. In the figure, the mass-weighted, global-average temperature $\langle T \rangle$ is steady in all the simulations presented, regardless of the drags employed in \mathcal{D} (black curve). With only the Newtonian drag applied in \mathcal{D} , the mass-weighted, global-average kinetic energy $\langle \mathcal{K} \rangle$ reaches steady state (at $t \approx 700$, red curve). With both drags not applied in \mathcal{D} , slow increase in $\langle \mathcal{K} \rangle$ is observed (green curve), but the rate of increase depends on time (and on the model setup). We stress that, in principle, such an evolution is physically valid – as long as $\langle \mathcal{K} \rangle$ does not ‘blow up’. Observe that the Rayleigh drag is responsible for suppressing the sensitivity (cf. orange, blue and red curves): for this, Newtonian drag by itself is ineffectual.

LS also suggest, following e.g. the study by Perna, Menou & Rauscher (2010) for higher altitude, that a Rayleigh drag in \mathcal{D} might serve as a crude representation of ‘magnetic drag effects’ stemming from thermal ionisation. There are two major concerns with this. First, thermal ionisation is insignificant in the \mathcal{D} region: temperature is too low and density is too high. This is so even taking into account the low ionisation potential of alkali metals (e.g. K, Na, Ca), as these are trace species (see e.g. Lewis 2004). Using solar abundances, $n_{H^+}/n_n \lesssim 2 \times 10^{-16}$ and $n_{K^+}/n_{H^+} \approx 3 \times 10^6$, where n_x is the x -specie number density and ‘n’ subscript refers to neutral. Hence, the bulk ionisation level (electron volume mixing ratio), $\chi_e \equiv n_e/n_n \approx n_{K^+}/n_n$, is at least 10^2 times lower than that required for the fluid medium to be influenced electromagnetically: $\chi_e \sim 10^{-7}$ is required for ionisation drag effects to become significant (e.g. Schunk & Nagy 2000; Koskinen et al. 2014). Second, even if the ion-induced drag were significant via a non-thermal mechanism, it cannot be represented as an *isotropic drag to rest* on the momentum¹⁵: ion velocities and the intrinsic field orientation need to be modeled self-consistently for accurate representation (e.g. Koskinen et al. 2010).

Let us now consider a more detailed look at the behaviour in time. Fig. 6 presents $t-p$ Hovmöller plots of the zonal velocity, $u(\lambda=0^\circ, \phi=30^\circ, p, t)$, for $t = [200, 300]$ and $\log(p) = [4.0, 7.3]$. Fig. 6a and 6b are from the simulations in Fig. 1c, which is at T85L40 resolution. Their general behaviours have been verified with up to T341L40 resolution using the BOB model. Fig. 6c presents a simulation with a setup identical to that of the simulation in Fig. 1a (East), except the resolution here is T21L1000

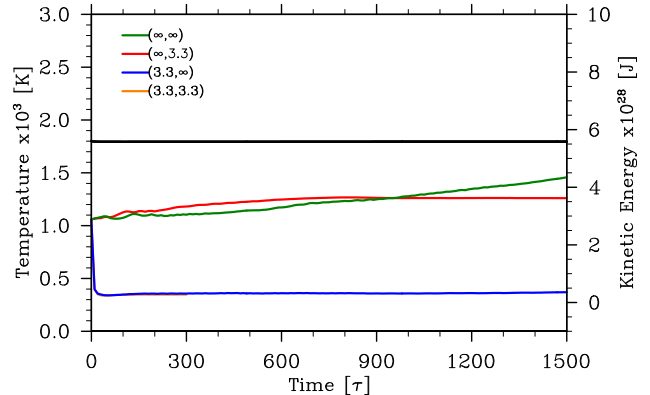


Figure 5. Mass-weighted, global-average temperature $\langle T \rangle$ (black) and kinetic energy $\langle \mathcal{K} \rangle$ (green, red, blue and orange) time series from four simulations set up identically, except for different (τ_{R20}, τ_N) in \mathcal{D} . When finite, $\tau_R(p)$ decreases linearly with p in $\log(p) = [5, 7.3] = [5, 6] \cup \mathcal{D}$ and τ_N is constant in \mathcal{D} ; outside their respective regions, $\tau_N(p)$ and $\tau_R(p)$ are as in LS in all cases. All are T85L40 BOB simulations, initialised with the $+1000 \text{ m s}^{-1}$ jet and $T_0 = 1800 \text{ K}$. The black curve is common to all four simulations. The blue and orange curves are very close to each other. The green and red curves are different for a different initialisation while the blue and orange curves are not.

($\Delta t = 8 \times 10^{-4}$ and $\nu_8 = 3 \times 10^{-10}$). The results are nearly identical at T42L500 and T85L40 resolutions. The simulation at T21L1000 resolution is presented here for equitable comparison with the simulation shown in Fig. 6d, in which the setup is identical to the simulation shown in Fig. 6c, except the vertical layers are now equally spaced in p . This spacing has the effect of representing the lower (higher) region with greater (fewer) number of layers: the resulting resolution in Fig. 6d, for example, is 57 times greater at the bottom of \mathcal{D} than that in Fig. 6c and in LS. In the simulation presented in Fig. 6d, the spacing is more numerically *consistent*¹⁶, as the equations solved in all the simulations are in p rather than $\log(p)$ coordinate.

Fig. 6a and 6b show vertically-propagating Rossby (planetary) waves, generally prominent in the model atmospheres when strong drags are not applied in \mathcal{D} . In the two panels, the waves are propagating in opposite directions (upward and downward in Fig. 6a and 6b, respectively), as evident from the tilt of the phase lines. The magnitude of the peak amplitude is $\sim 700 \text{ m s}^{-1}$ in both, given the latitude location of the constructed plots, but the sign and period are different – as is the growth with height over time. As already discussed, such waves can induce significant modification of the background flow via saturation and encounter with critical layers (e.g. Andrews et al. 1987; Holton 2004). The action of the waves will be discussed more in detail elsewhere. Here we wish to highlight the suppression of essentially *all* temporal activity – including these waves – when the strong drags are applied in \mathcal{D} , in addition to a strong Newtonian drag already applied throughout nearly all of the domain outside \mathcal{D} (cf. Fig. 6c with Fig. 6b). While not uninteresting, such a ‘dead’ atmosphere shown in Fig. 6c is not dynamic, and a flow simulation of it is not very informative.

Interestingly, the suppressed behaviour is not robust and appears to be a numerical artifact. This is demonstrated in Fig. 6d.

¹⁵ This is also true of gravity wave induced drag.

¹⁶ Numerical consistency refers to discretisation error tending to zero as the resolution is increased, under pointwise convergence at each grid point (e.g. Strikwerda 2004).

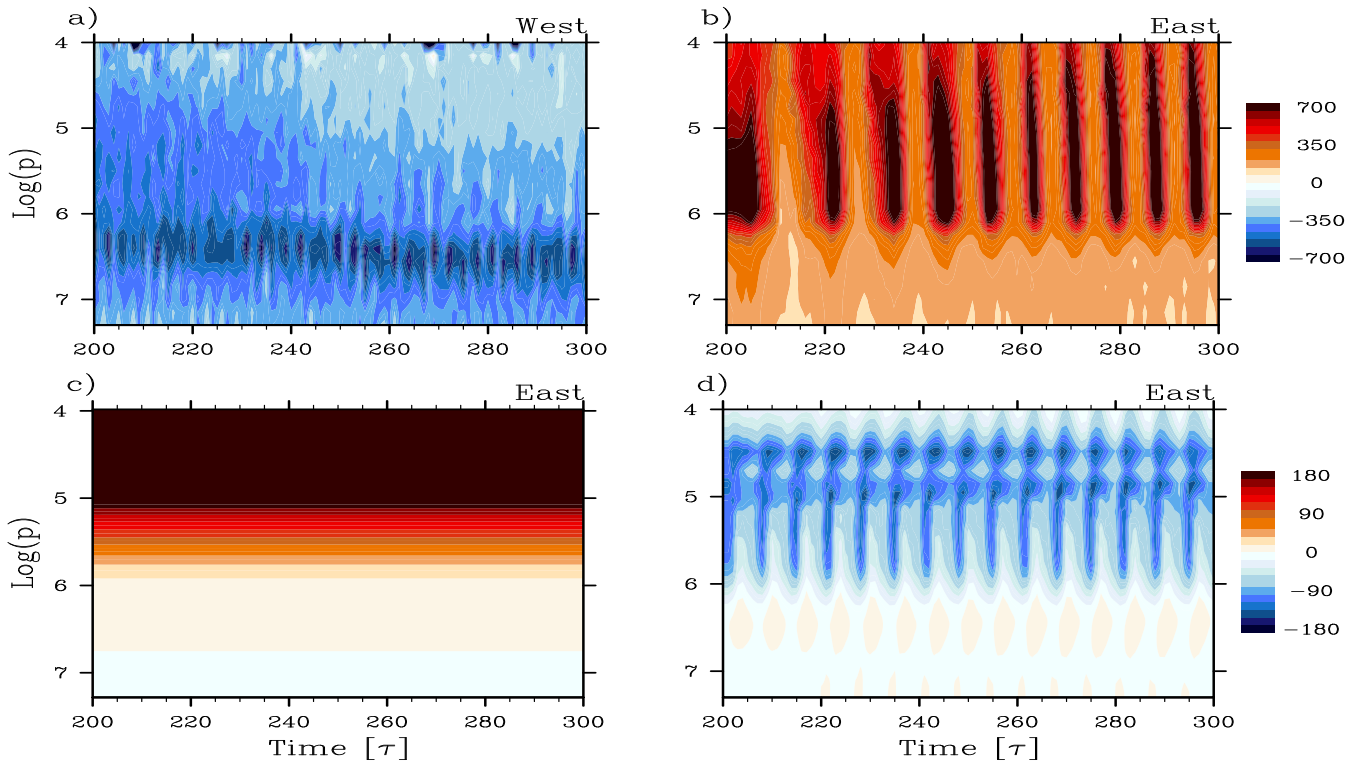


Figure 6. t - p Hovmöller plots of instantaneous zonal velocity $u(t,p)|_{(\lambda,\phi)=(0,30)}$ for $t = [200, 300]$ and $\log(p) = [4.0, 7.3]$. The colour bars indicate the velocity for each row. All simulations are performed with BOB. Initial jet amplitudes and directions (indicated above each plot) are as in Fig. 1. In a) and b), the resolution is T85L40 and $\tau_{R20}, \tau_N \rightarrow \infty$ in \mathcal{D} . In c) and d), the resolution is T21L1000 and $\tau_{R20}, \tau_N \rightarrow 3.3$ in \mathcal{D} (as in LS) with the vertical levels equally-spaced in $\log(p)$ (c) and p (d). Vertically-propagating waves of planetary scale power variability and behave differently, depending on the initial flow, when strong drags are not applied in \mathcal{D} [cf. a) and b)]. However, even with the strong drags employed, propagating waves are present if the vertical resolution is increased in \mathcal{D} [cf. c) and d)].

The panel shows the behaviour of the simulation in Fig. 6c when the vertical resolution of the dynamically active region ($\log(p) \approx [5, 6]$) is increased, principally by employing a different spacing. As can be seen in Fig. 6d, the variability returns – powered by waves that strongly shear, emerging from the \mathcal{D} region, and induce secondary and even tertiary waves upon interacting strongly with the northern flank of the equatorial jet at $\log(p) \approx [5.0, 4.5]$ (see Fig. 1a). The amplitude of the waves here is much smaller than those in Fig. 6a and 6b, consistent with the much stronger drag in this case. Propagating gravity waves that are similarly generated can enhance the observed variability as well (e.g. Scinocca & Ford 2000; Watkins & Cho 2010), but these waves are poorly captured in this simulation at the employed resolution.

4 CODA

We close with some thoughts and observations arising from this study. We have carefully cross-checked the results with codes used in TC and LS, as well as a third code (which has been extensively tested under conditions appropriate for hot-Jupiters). As shown by Polichtchouk et al. (2014) and the present study, one can arrive at erroneous conclusions if simulations from different codes are not at least qualitatively reproduced *with the same setup*. Even then, erroneous conclusions can still be drawn, as codes which perform well ostensibly in one region of the physical parameter space do not

perform well in another (or, more precisely, extended) region. For example, when pushed to a highly ageostrophic¹⁷ region (as would occur in a typical hot-Jupiter atmosphere simulation), numerical accuracy of the code can become seriously degraded by small-scale oscillations generated in that region of the parameter space (e.g. Thrastarson & Cho 2011).

By expanding the study by Polichtchouk et al. (2014) into the *initial condition space*, the results here constitute an extension of that study: in general, simulations are sensitive to initial condition – in addition to many other factors, physical and numerical. That the physical system under study exhibits multiple equilibrium states (hence, also non-ergodicity) is not, it seems to us, a particularly startling assertion given its highly nonlinear and poorly constrained forced-dissipative nature. But, it has been challenged forcefully by LS.

Ultimately, it appears the question of sensitivity and variability rests on whether one believes that it is truly ‘realistic’ to apply Rayleigh drag as well as Newtonian drag on very short timescales, particularly in the \mathcal{D} region. Even assuming that the drags are acceptable representations of the forcing and dissipation in hot-Jupiter atmospheres, one must ask: how realistic are τ_N , τ_R and T_e currently used? The responses of TC and LS clearly differ on this question. A telling observation of this study is the extraordinary

¹⁷ e.g. high Rossby and Froude numbers – measures of rotation rate and stratification, respectively (see e.g. Holton 2004)

length one must go to suppress sensitivity and variability inherent in the system: *all eddies and waves must be eliminated for all time*. One may wonder whether such a state is really realistic, given that the atmosphere would likely contain some vorticity and turbulence (both inhomogeneous and intermittent) and that there are altitude regions (e.g. just above \mathcal{D}) characterised by neither short Newtonian nor short Rayleigh drag timescales. In our view, the general question of realistic forcing and initialisation – and their effects – is still unsettled, and the question deserves much more attention and scrutiny than has generally received thus far.

Most importantly, the investigation should proceed with the following observations squarely in the fore. We have found that MITgcm in the cubed-sphere grid configuration conserves angular momentum poorly and is acutely sensitive to numerical parameter values in simulations initialised with high speed jets, particularly without the strong Rayleigh drag applied in \mathcal{D} (e.g. Fig. 2): hence, it cannot be used for assessing sensitivity in this case, as it is not possible to establish a reliable baseline for quantification. We have also found that, *all* codes used in this study (including BOB) lead to a zonally-symmetric, superrotating, supersonic jet at the equator, at $\log(p) \approx 3$. Given that the hydrostatic primitive equations with free-slip boundary conditions (as well as with the viscosity representation for small Mach number flows) are solved in all the numerical models in this study, such flow is physically not valid [see e.g. discussion in Holton (2004)]. Therefore, claims of realism in these setups is moot: such jets may occur on real hot-Jupiters, but not in these simulations. Either a different setup must be used for the equations and boundary conditions solved *or* a different set of equations and boundary condition must be solved for the setup used. Relatedly, while all of the simulations presented *here* exhibit supersonic zonally-symmetric equatorial flow at some height, not all simulation do: in general, that depends on the physical setup, numerical scheme and initial condition employed (e.g. Thrastarson & Cho 2010; Polichtchouk et al. 2014).

ACKNOWLEDGMENTS

The authors acknowledge helpful discussions with Craig Agnor, Tommi Koskinen and Stephen Thomson – and particularly for their careful reading of the manuscript. The authors also acknowledge the hospitality of the Kavli Institute for Theoretical Physics, Santa Barbara, where some of this work was completed. I.P. is supported by UK’s Science and Technology Facilities Council research studentship. H.Th.Th. is supported by the NASA Post-doctoral Program at the Jet Propulsion Laboratory, administered by Oak Ridge Associated Universities through a contract with NASA.

REFERENCES

Adcroft A. et al., 2012, ‘MITgcm User Manual’
 Andrews, D. J., Holton J. R., Leovy, C., 1987, Middle Atmosphere Dynamics, Academic Press, San Diego)
 Bending V. L., Lewis S. R., Kolb U., 2012, MNRAS, 428, 2874
 Brandefelt J., Otto-Bliesner B. L., 2009, GRL, 36, L19712
 Cho J. Y-K., Menou K., Hansen B. M. S., Seager S., 2003, ApJ, 587, L117
 Cho J. Y-K., Menou K., Hansen B. M. S., Seager S., 2008, ApJ, 675, 817
 Collins W. D. et al., 2004, Description of the NCAR Community Atmosphere Model (CAM 3.0)
 Cooper C. S., Showman A. P., 2005, ApJ, 629, L45
 Dobbs-Dixon, I., Lin, D. N. C., 2008, ApJ, 673, 513
 Ford, R., McIntyre, M. E., Norton, W., A. 2000, J. Atmos. Sci., 57, 1236
 Held I. M., Suarez M. J., 1994, Bull. Amer. Met. Soc., 75, 1825
 Heng, K., Menou, K., Phillipps, P., 2011, MNRAS, 413, 2380
 Holton J. R., 2004, Introduction to Dynamic Meteorology, 4th ed., Academic Press, San Diego
 Koskinen T., Cho J. Y-K., Achilliios N., Aylward A. D. 2010, ApJ, 722, 178
 Koskinen T., Yelle, R., Lavvas, P., Cho J. Y-K. 2014, ApJ, 796, 16
 Knutson H. A., Charbonneau, D., Allen, L. E., Fortney, J. J., Agol, E., Cowan, N. B., Showman, A. P., Cooper, C. S., Megeath, S. T., 2007, Nature, 447, 183
 Lewis J. S., 2004, Physics and Chemistry of the Solar System, 2nd ed., Academic Press, Amsterdam
 Liu B., Showman A. P., 2013, ApJ, 770, 42
 Mayne,N. J., Baraffe, I., Acreman, D. M., Smith, C. Browning, M. K., Amundsen, D. S., Wood, N., Thuburn, J., Jackson, D. R., 2014, A& A, 561, 24
 Munkres J. R., 2000, Topology, 2nd ed., Prentice Hall, Upper Saddle
 Perna, R., Menou, K., Rauscher, E., 2010, ApJ, 719, 1421
 Polichtchouk, I., Cho Y-K. J., 2012, MNRAS, 424, 1307
 Polichtchouk, I., Cho Y-K. J., Watkins C., Thrastarson H. Th., Umurhan O., Juarez, M. T., 2014, Icarus, 229, 355
 Salby M. L., 2000, Fundamentals of Atmospheric Physics, Academic Press, San Diego
 Schneider T., Liu J., 2009, JAS, 66, 579
 Schunk, R. W., Nagy, A. F. 2000, Ionospheres: Physics, Plasma Physics, and Chemistry, Cambridge University Press, Cambridge
 Scott R. K., Rivier L., Loft R., Polvani L. M., 2004, NCAR Technical Note No. 456
 Scinocca J. F., Ford, R. 2000, J. Atmos. Sci., 57, 653
 Showman A. P., Fortney J. J., Lian Y., Marley M. S., Freedman R. S., Knutson H. A., Charbonneau D., 2009, ApJ, 699, 564
 Strikwerda, J. C., 2004, Finite Difference Schemes and Partial Differential Equations, 2nd ed., SIAM, Philadelphia
 Thrastarson H. Th., Cho J. Y-K., 2010, ApJ, 716, 144
 Thrastarson H. Th., Cho J. Y-K., 2011, ApJ, 729, 117
 Watkins C., Cho J. Y-K., 2010, ApJ, 714, 904